



## REVIEW ARTICLE

# Adsorption of $Cd^{2+}$ and $Pb^{2+}$ by biofuel ash-based geopolymer synthesized by one-step hydrothermal method



Jingmin Wan<sup>a,b</sup>, Fawang Zhang<sup>c,\*</sup>, Zhantao Han<sup>d,\*</sup>, Le Song<sup>e</sup>, Chaoyue Zhang<sup>b</sup>, Jiasen Zhang<sup>b</sup>

<sup>a</sup> Institute of Karst Geology, CAGS, Guilin 541004, China

<sup>b</sup> School of Water Resources and Environment, Hebei GEO University, Key Laboratory of Sustained Development and Utilization of Water Resources, Shijiazhuang 050031, China

<sup>c</sup> Center For Hydrogeology and Environmental Geology Survey, CGS, Baoding 071051, China

<sup>d</sup> Technical Centre for Soil, Agriculture and Rural Ecology and Environment, Ministry of Ecology and Environment, Beijing 100012, China

<sup>e</sup> Hebei and China Geological Survey Key Laboratory of Groundwater Remediation, Institute of Hydrogeology and Environmental Geology, Chinese Academy of Geological Sciences, Shijiazhuang 050061, China

Received 26 February 2021; accepted 19 May 2021

Available online 26 May 2021

## KEYWORDS

Biofuel ash;  
Hydrothermal method;  
Geopolymer;  
Heavy metal adsorption

**Abstract** A hydrothermal alkali modification method was used to produce geopolymer (BFA-GP) from biofuel ash (BFA). The product was characterized by scanning electron microscopy with energy dispersive spectrometry (SEM-EDS), transmission electron microscopy (TEM), X-ray diffraction (XRD), Fourier transform infrared reflection (FTIR), and X-ray photoelectron spectroscopy (XPS). Significant amount of geopolymer and gismondine was produced by this modification. The surface area increased from 20.41 m<sup>2</sup> g<sup>-1</sup> to 56.63 m<sup>2</sup> g<sup>-1</sup>. The adsorption capacity of BFA-GP can reach 29.92 and 137.49 mg g<sup>-1</sup> for Cd<sup>2+</sup> and Pb<sup>2+</sup>, respectively, in a pure solution at 298 K, which is about triple of that by the original BFA. Competitive adsorption of Cd<sup>2+</sup> and Pb<sup>2+</sup> showed that the binding affinity is Pb<sup>2+</sup> > Cd<sup>2+</sup>. Chemical sorption including electrostatic attraction, chelate reaction, and ion-exchange is the dominant mechanism of heavy metal adsorption on BFA-GP. And the adsorption thermodynamics indicates that adsorption reaction of heavy metal ions by BFA-GP is spontaneous and endothermic. This modification provided a

\* Corresponding authors.

E-mail addresses: [fawangzhang1965@sina.com](mailto:fawangzhang1965@sina.com) (F. Zhang), [hanzhantao@tcare-mee.cn](mailto:hanzhantao@tcare-mee.cn) (Z. Han).

Peer review under responsibility of King Saud University.



cost-effective and environmentally friendly way to change BFA to adsorbent for heavy metals with promising application prospects.

© 2021 Published by Elsevier B.V. on behalf of King Saud University. This is an open access article under the CC BY-NC-ND license (<http://creativecommons.org/licenses/by-nc-nd/4.0/>).

## Contents

1. Introduction . . . . .	2
2. Materials and methods . . . . .	3
2.1. Materials . . . . .	3
2.2. Modification of BFA . . . . .	3
2.3. Characterization . . . . .	3
2.4. Adsorption experiments . . . . .	4
3. Results and discussion . . . . .	4
3.1. Characterization of BFA-GP . . . . .	4
3.1.1. Mineral composition . . . . .	4
3.1.2. Microstructural characteristics and surface area . . . . .	4
3.1.3. FTIR and XPS analysis . . . . .	6
3.1.4. Zeta potential and zero charge point . . . . .	7
3.2. Comparison of Cd <sup>2+</sup> adsorption on BFA-GP and BFA . . . . .	8
3.3. Effect of pH . . . . .	8
3.4. Characterization of adsorption kinetics . . . . .	9
3.5. Adsorption isotherms of Cd <sup>2+</sup> and Pb <sup>2+</sup> on BFA-GP . . . . .	12
3.5.1. Adsorption isotherms in pure solution . . . . .	12
3.5.2. Competitive adsorption . . . . .	12
3.6. Adsorption thermodynamics of Cd <sup>2+</sup> and Pb <sup>2+</sup> on BFA-GP . . . . .	13
3.7. Mechanism of Cd <sup>2+</sup> and Pb <sup>2+</sup> adsorption on BFA-GP . . . . .	13
4. Conclusion . . . . .	14
Funding . . . . .	14
Declaration of Competing Interest . . . . .	15
References . . . . .	15

## 1. Introduction

Wastewater contains high concentrations of soluble heavy metal ions discharged from many industries such as mining, metallurgy, and battery manufacturing (Xu et al., 2020, Shao et al. 2020a), which has led to contamination of groundwater and soil (Lin et al. 2020a). Heavy metals are one of the most hazardous materials due to their high toxicity and persistence (Qiao et al. 2020, Lin et al. 2020b).

Techniques used to remove heavy metals from water include chemical precipitation (Duarte-Nass et al. 2020), ion exchange (Nekouei et al. 2019), membrane filtration (Bai, Wang and Zhu 2020), and adsorption (Di Natale, Gargiulo and Alfe 2020). Adsorption has been proposed due to the advantages of easy operation, cost-effectiveness, and extensively available adsorbent materials (Xu et al. 2020). These are widely used in the treatment of heavy metal-contaminated water (Wieszczycka et al. 2020, Fakhre and Ibrahim 2018). Adsorbents include activated carbon (Shahrokhi-Shahraki et al. 2020), natural zeolites (Hong et al. 2019), fly ash (Alinnor 2007), and other industrial and agricultural wastes (Shao et al. 2020b) and organic materials such as resins and alginate hydrogels (Jiang et al. 2020). Among them, industrial waste-derived materials are one the most promising adsorbents for metal ions adsorption due to

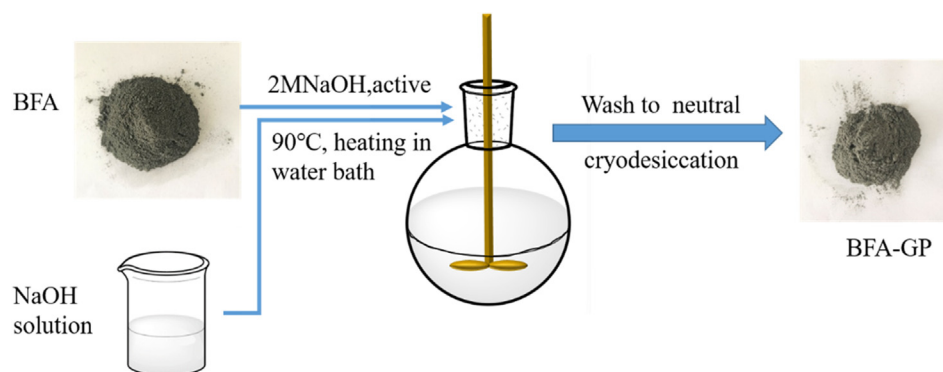
their high adsorption capacity and low cost. (Di Natale et al. 2020).

In recent years, geopolymers have attracted much attention as a new heavy metal adsorbent (Siyal et al. 2018, Chen et al. 2019b, Rasaki et al. 2019). Geopolymers are inorganic polymeric materials with a three-dimensional porous structure synthesized from industrial wastes or mineral materials containing aluminosilicate through alkaline activation (Khale and Chaudhary 2007). Geopolymers have high adsorption ability due to their large specific surface area, porous structure, and abundant surface functional groups (Tan et al. 2020). They also have good mechanical properties and thermal/chemical stability versus organic adsorbents (Chen et al. 2019a). Geopolymers have been widely used in heavy metals (Darmayanti et al. 2019) and dye (Barbosa et al. 2018) removal from liquid as well as VOCs (Tang et al. 2020) adsorption from waste gas. But most of the method to produce geopolymer needs long curing time (> 10 days) (Andrejkovičová et al., 2016; Yousef et al., 2009; Huang and Han 2011), which is very costly in practice.

Precursor materials for the preparation of geopolymers include fly ash (Onutai et al. 2019, Wang et al. 2020), metakaolin (Cheng et al. 2012, Kara, Yilmazer and Akar 2017, Tian, Guo and Sasaki 2020), red mud (Chen et al. 2019b) and other industrial byproducts containing aluminosilicate (Chen et al.

**Table 1** Chemical composition of BFA and BFA-GP.

Composition	Content(%)							
	SiO <sub>2</sub>	Al <sub>2</sub> O <sub>3</sub>	CaO	Fe <sub>2</sub> O <sub>3</sub>	MgO	Na <sub>2</sub> O	P <sub>2</sub> O <sub>5</sub>	K <sub>2</sub> O
BFA	47.26	12.67	19.19	7.49	3.86	1.19	1.07	4.20
BFA-GP	51.9	15.4	11.79	5.60	3.12	3.3	0.579	2.08

**Fig. 1** Schematic map showing BFA-GP synthesis.

2019a, Sarkar, Basu and Samanta 2019, Sha, Pan and Sun 2020). In the past years, large amount biomass power plants have been built up in China as a new way to produce renewable energy (Qin et al. 2018). It is estimated that 480 million tons of BFA will be produced by 2050 worldwide (Stanislav V. Vassilev et al. 2013). Thus, the disposal and utilization of BFA has become a challenging task worldwide. The main elements in BFA are silica, aluminum, oxygen, calcium, potassium, and other metals (Shi et al. 2017). The content of silica and aluminum oxide in BFA can reach more than 60%, making BFA a suitable precursor material for preparing geopolymer. Pérez-Villarejo et al. (2018) prepared geopolymers using biomass fly ash and aluminum industrial slag activated by a mixture of sodium hydroxide and sodium silicate. Novais et al. (2019) synthesized geopolymer from biomass fly ash by injecting FA slurry into a polyethylene glycol medium (85 °C) and curing at room temperature for 27 days. Based on these studies, we designed a fast hydrothermal alkali modification method to produce geopolymer by BFA, and the produced geopolymer was testified has superior adsorption capacity for Cd<sup>2+</sup> and Pb<sup>2+</sup> which are very popular heavy metal contaminants in China. It's expected the BFA-GP could be widely used in the heavy metal wastewater treatment and heavy metal contaminated soil remediation.

## 2. Materials and methods

### 2.1. Materials

BFA used in this study obtained from the bottom of a boiler that produces electricity by burning several kinds of biomass as fuel in JinZhou biomass power plant (Shijiazhuang, China). XRF test results are listed in Table 1.

Analytical reagent (AR) grade sodium hydroxide (NaOH), hydrochloric acid (HCl), cadmium nitrate (Cd(NO<sub>3</sub>)<sub>2</sub>·2H<sub>2</sub>O),

lead nitrate (Pb(NO<sub>3</sub>)<sub>2</sub>) were purchased from Tianjin, China. All the water used in the experiment was ultrapure water.

### 2.2. Modification of BFA

BFA was ground to ≤ 74 μm and subsequently washed by ultrapure water until the conductivity was constant. It was then oven dried at 105 °C overnight.

Geopolymer was synthesized by one-step hydrothermal alkali modification method as shown in Fig. 1. A fixed amount of BFA was mixed with 2 M NaOH at solid-liquid ratio of 1:15. The resulting mixture was fed into a round flask and heated in a 90 °C water bath with stirring for 12 h. The material was cooled naturally followed by aging for 2 h at ambient temperature and separated by centrifugation. The solid products were washed three time by deionized water, and freeze dried for 48 h. The solid was sieved to the particle size of ≤ 74 μm, and the final sample was called BFA -GP.

### 2.3. Characterization

Scanning Electron Microscope with Energy Dispersive Spectrometer (SEM- EDS, ProX, Phenom, Holland) was utilized to observe the microscopic morphology and chemical elements of BFA and BFA-GP. Transmission electron microscopy (TEM) characterization was carried out by a TEM/STEM FEI Tecnai F30 microscope. The surface area, total pore volume and pore size distribution were measured through N<sub>2</sub> adsorption-desorption method at approximately 77.3 K using Automatic Surface Area and Porosity Analyzer (ASAP 2460, Micromeritics, USA). The specific surface areas of BFA and BFA-GP were determined for the relative pressure range of 0.0–1.0 and calculated by the Brunauer-Emmette-Teller (BET) method. The total pore volume was determined for a single point P/P<sub>0</sub> value of 0.990. The pore size distributions

of the samples were inferred from the adsorption isotherms by means of the Barrett-Joyner-Halenda (BJH) method. Before testing, the sample was degassed at 200 °C for 6 h. Mineral composition of BFA and BFA-GP was obtained by X-ray diffraction (XRD, D8 Advance, Bruker, Germany) using Cu-K $\alpha$  radiation with a wavelength of 1.5406 Å, tube voltage and current are 40 KV and 40 mA, respectively. The range of XRD patterns was from 2 $\theta$  of 10° to 80° with a scanning rate at 1.5°/min. The functional groups in BFA-GP were probed using Fourier-transform infrared spectroscopy (FTIR, iS10, Nicolet, USA) by KBr pelletized technique. Each spectrum in the 4000–400 cm<sup>-1</sup> range was accumulated from 32 individual scans. The chemical components of samples were characterized by X-ray photoelectron spectroscopy (XPS) using a Thermo escalab 250XI spectrometer with monochromatic Al K $\alpha$  radiation. The zeta potential of the geopolymer was measured at different pH (1–9) using Zeta-sizer instrument (MALVERN, UK) to calculate the point of zero charge (pHZPC).

#### 2.4. Adsorption experiments

The solutions contained 320 mg L<sup>-1</sup> of Cd<sup>2+</sup> and 1600 mg L<sup>-1</sup> of Pb<sup>2+</sup> were prepared by dissolving the corresponding nitrate salts Cd(NO<sub>3</sub>)<sub>2</sub>·2H<sub>2</sub>O and Pb(NO<sub>3</sub>)<sub>2</sub> in deionized water, and diluted to the desired concentration in subsequent experiments.

Batch experiments were carried out to get the equilibrium adsorption data of Cd<sup>2+</sup> or Pb<sup>2+</sup> or their mixture onto BFA-GP. The experimental procedures are described as following: 0.1 g BFA-GP was put into a 50-mL Teflon centrifuge tube, 40 mL solution containing Pb<sup>2+</sup> or Cd<sup>2+</sup> or their mixture with different concentrations was then added. The pH of mixture solution was adjusted to 6.5 ± 0.2 with 0.1 M HCl or NaOH and the tubes were sealed with screw caps. All samples were prepared in duplicate. The Teflon centrifuge tubes were shaken at 298 K and 150 rpm for 24 h. After shaking, the mixtures were centrifuged at 3000 rpm for 10 min and then filtered through a 13-mm syringe filter with a 0.45- $\mu$ m membrane. The supernatants were collected and the metal ion concentrations were measured by atomic absorption spectrophotometry (AA-7000, Shimadzu, Japan).

Kinetic adsorption were performed by adding 40 mL 400 mg L<sup>-1</sup> Pb<sup>2+</sup> or 80 mg L<sup>-1</sup> Cd<sup>2+</sup> solutions, or their mixture into eighteen 50-mL Teflon centrifuge tubes. The pH of mixture solution was adjusted to 6.5 ± 0.2 with 0.1 M HCl or NaOH and sealed with screw caps. The samples were shaken at 298 K and 150 rpm and at determined time intervals, 2 samples were collected, centrifuged and the supernatant were filtered and the metal ion concentrations were measured by the same method as in equilibrium adsorption.

Another set of adsorption experiments were performed to investigate the adsorption thermodynamics. Three pairs of samples were prepared as in previous steps: 40 mL Pb<sup>2+</sup> and Cd<sup>2+</sup> in the range of 20–800 mg L<sup>-1</sup> and 2–160 mg/L and 0.1 g BFA-GP were put into 50-mL Teflon centrifuge tubes, the pH of sample solution was adjusted to 6.5 ± 0.2 with 0.1 M HCl or NaOH and the tubes were sealed with screw caps, but were shaken under different temperatures (298 K, 308 K, and 318 K) for 24 h before centrifugation and measure the Pb<sup>2+</sup> and Cd<sup>2+</sup> concentrations in supernatants.

The adsorption at equilibrium ( $q_e$ , mg g<sup>-1</sup>) were determined according to Eq. (1):

$$q_e = \frac{(C_0 - C_e)}{m} \cdot V \quad (1)$$

where  $C_0$  and  $C_e$  represent the initial and equilibrium concentrations of heavy metal ions in solution, respectively (mg · L<sup>-1</sup>);  $V$  is the volume (L) of the solution;  $m$  is the adsorbent mass (g).

### 3. Results and discussion

#### 3.1. Characterization of BFA-GP

##### 3.1.1. Mineral composition

X-ray diffraction (XRD) was used to detect the mineral composition of BFA and BFA-GP. The XRD spectrograms of BFA and BFA-GP are shown in Fig. 2. The main minerals in BFA is quartz (JCPDS No: 46-1045) and margarite (JCPDS No: 18-0276) with some CaCO<sub>3</sub>. The amorphous halo between 2 $\theta$  20° and 35° observed in the BFA XRD pattern is the characteristic of amorphous nature of biofuel ash (Siyal et al. 2016, Hui-Teng et al. 2021). After modification, the intensity of the diffraction peak of quartz at 2 $\theta$  = 20.8° decreased, and the peak of margarite at 2 $\theta$  = 27.9° disappeared, indicating that some of the quartz and all the margarite in the BFA dissolved during the modification. The broad peak around 2 $\theta$  between 20° and 35° in the XRD pattern of BFA-GP may be attributed to the presence of amorphous geopolymer (Singhal, Gangwar and Gayathry 2017). The diffraction peak at 2 $\theta$  = 26.6° which is belongs to both quartz and gismondine (JCPDS No: 20-0452) intensified, and a new peak appear at 2 $\theta$  = 36.5° which is belongs to gismondine. The formation of gismondine is very favorable for heavy metal cations adsorption due to the presence of the ion exchange centers in zeolite where Al and Si tetrahedra are connected.

##### 3.1.2. Microstructural characteristics and surface area

Fig. 3 presents SEM images of BFA and BFA-GP, and their corresponding energy dispersive spectrometry. By comparing Fig. 2(a) and (b), many cracks and opening pores and some

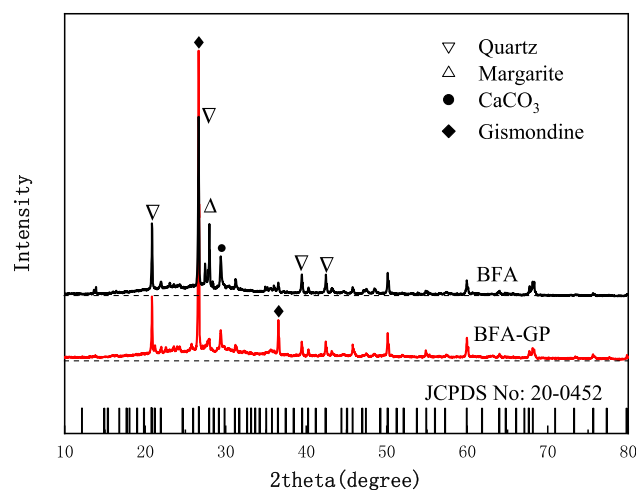


Fig. 2 XRD patterns of BFA and BFA-GP.

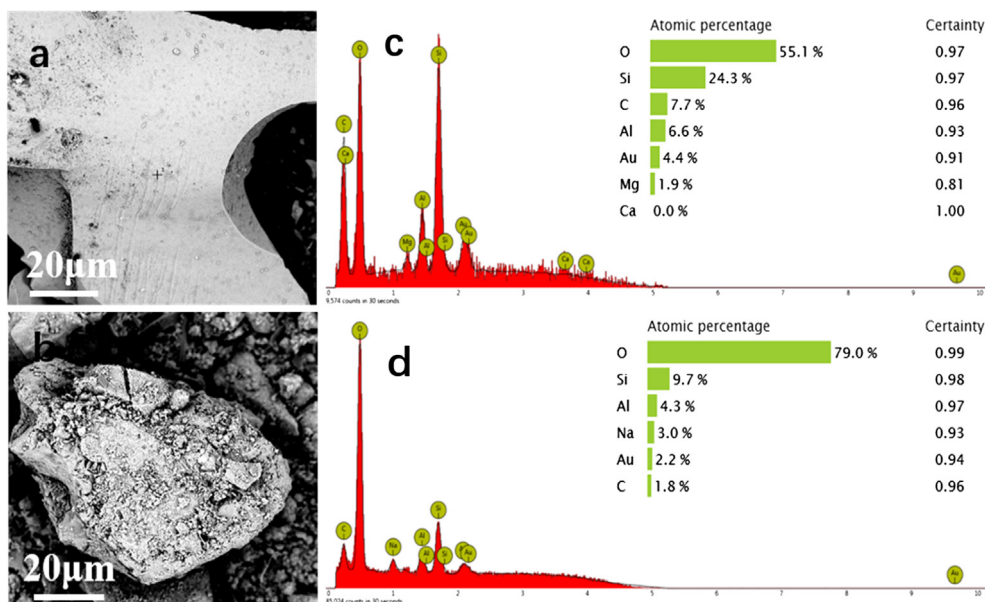


Fig. 3 SEM micrographs of BFA (a), BFA-GP (b) and EDS analysis of BFA (c), BFA-GP (d).

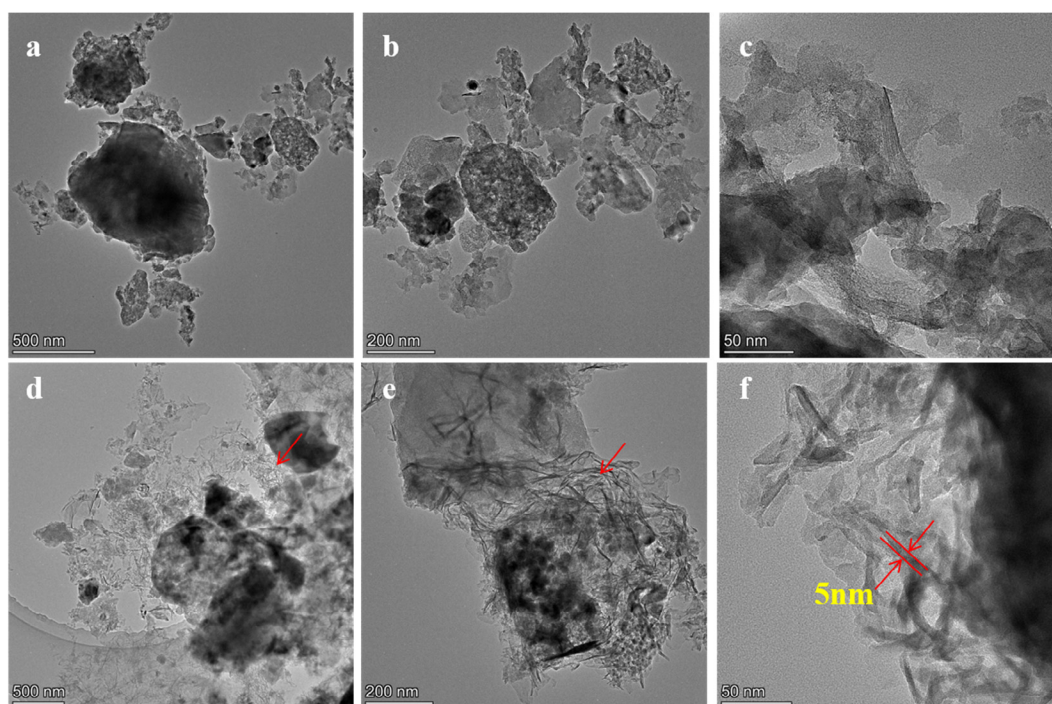
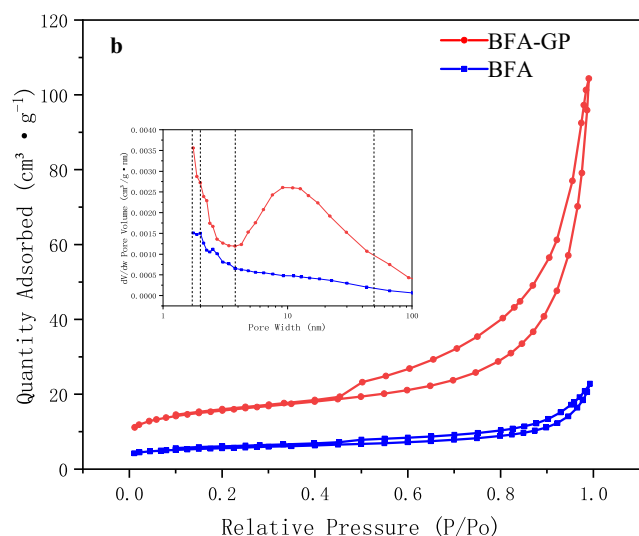


Fig. 4 TEM images of BFA (a, b, c) and BFA-GP (d, e, f) at different magnifications.

small particles were produced by the modification. The change in the morphology of the product likely causes a significant increase in the specific surface area as shown in Fig. 2(b).

As demonstrated in Fig. 2(c, d), the main elements of BFA and BFA-GP were O, Si and Al. But a Na peak appeared in the spectrum of BFA-GP which come from NaOH solution, indicating that alkali activator participated in the modification and Na ions were fixed into BFA-GP. Similar results have been reported in previous literature (Sha et al. 2020).

The microstructure of BFA and BFA-GP were shown in high-resolution TEM images (Fig. 3). Many spherical particles of around 100–800 nm were observed in BFA as shown in Fig. 4(a)–(b). But in the images of BFA-GP, many fiber-like gismondine crystals with diameter of around 5 nm can be clearly observed (Fig. 4(d)–(f)). The morphology of geopolymer prepared by biofuel ash is different from that by coal bottom ash (Santa et al. 2021). This may be due to the varied Si/Al ratio of raw material and different polymerization conditions



**Fig. 5**  $N_2$  adsorption-desorption isotherm curves of BFA and BFA-GP.

(Rożek, Król and Mozgawa 2019). Potassium salt and sodium salt in raw biofuel ash were dissolved during washing.

The  $N_2$  adsorption-desorption isotherms of BFA and BFA-GP are displayed in Fig. 5. The specific surface area ( $S_{BET}$ ), total open pore volume at  $P/P_0 = 0.99(V_T)$ , t-Plot micropore volume ( $V_{mic}$ ), and BJH desorption average pore width of BFA and BFA-GP were determined by  $N_2$  adsorption-desorption test. The surface area of the BFA increased from  $20.41 \text{ m}^2 \text{ g}^{-1}$  to  $56.63 \text{ m}^2 \text{ g}^{-1}$  after modification; meanwhile, the total open pore volume also increased from  $0.0337 \text{ cm}^3 \text{ g}^{-1}$  to

$0.1600 \text{ cm}^3 \text{ g}^{-1}$ , and the pore size increased from 12.5 nm to 13.6 nm. The increase in specific surface area and pore volume may be due to the dissolution and rearrangement of aluminosilicate, which resulted in new pores and small particles as seen in the SEM and TEM images (Fig. 3 and Fig. 4). The specific surface area is generally considered to be the most important property determining the adsorption capacity (Liu et al. 2016).

Usually, the characteristic pores in the material can be judged by the shape of the adsorption curve and the hysteresis loop. The adsorption curves of BFA and BFA-GP were type IV adsorption curves and were mostly produced by mesoporous substances. Moreover, according to the classification of international union of pure and applied chemistry (IUPAC), the hysteresis loop of BFA-GP was Type H3 type indicating that there were slit-like pores in the material. The pore size distributions of BFA and BFA-GP were displayed in the insert graph of Fig. 5. There were two main differences in pore size distribution between BFA-GP and BFA. One was the increase in pore width less than 2 nm, which may result from the formation of gismondine. Another significant difference was the pore width of 3–50 nm in the BFA-GP increased drastically. This change could be attributed to the formation of geopolymer identified as a mesoporous material with a characteristic pore size between 2 and 50 nm (Siyal et al. 2018).

### 3.1.3. FTIR and XPS analysis

FTIR spectra of BFA, BFA-GP, and BFA-GP after adsorption of Cd (BFA-GP-Cd) are shown in Fig. 6 (a). The comparison of BFA-GP with BFA shows some changes in the adsorption band. The broad absorption band around  $3440 \text{ cm}^{-1}$  and the peak near  $1630 \text{ cm}^{-1}$  represent asymmetric

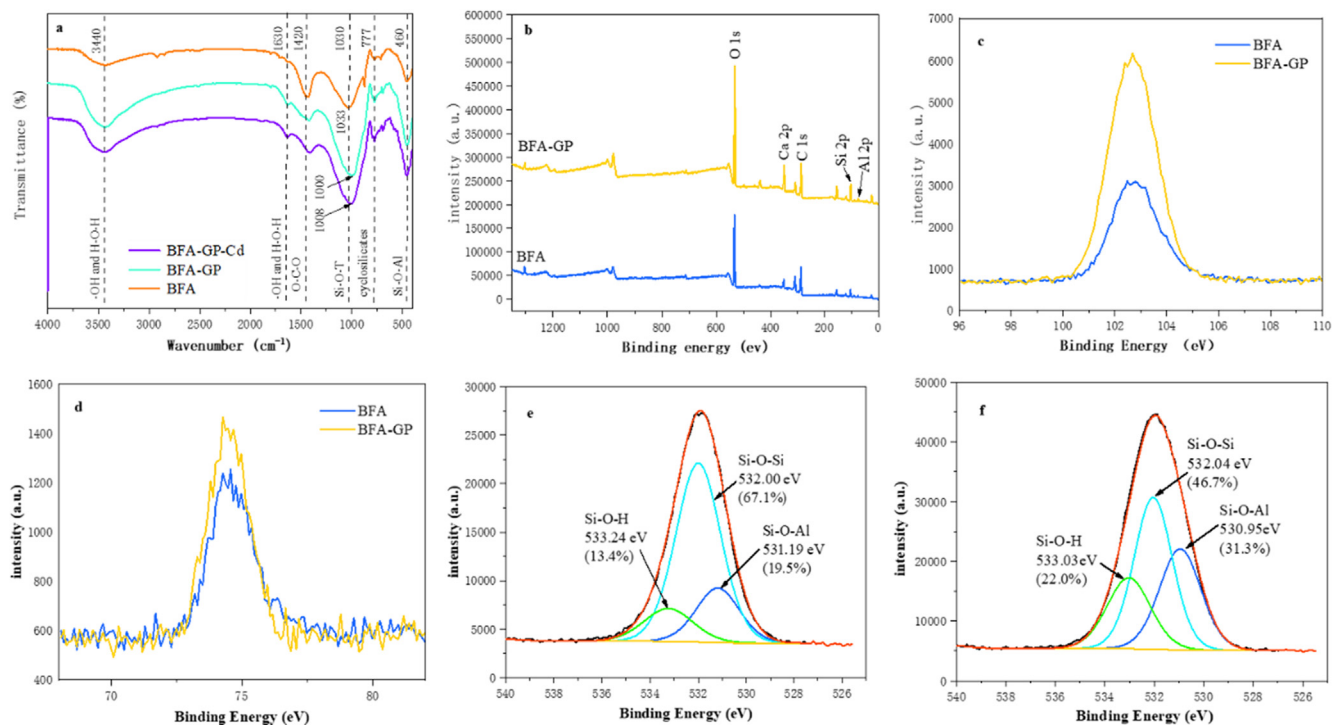


**Fig. 6** FTIR spectrum of the BFA, BFA-GP and BFA-GP-Cd (a) and XPS spectra of BFA and BFA-GP: (b) wide scan, (c) Si 2p spectra, (d) Al 2p spectra, (e) O 1s high resolution XPS spectra of BFA, (f) O 1s high resolution XPS spectra of BFA-GP.

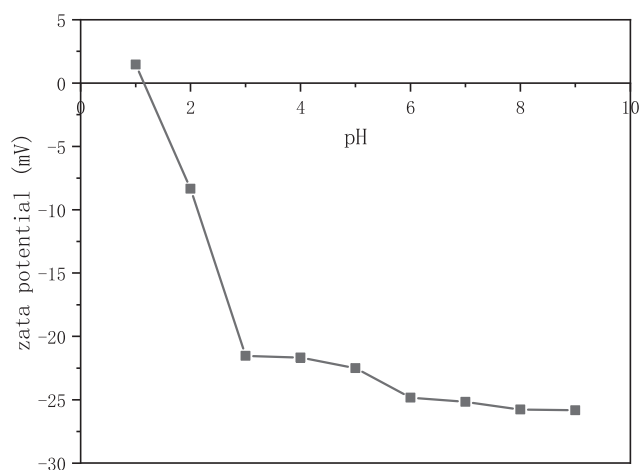


**Fig. 7** Zeta potentials of BFA-GP sample under different pH conditions.

stretching vibration and deformational vibrations of H—O—H and —OH bond (Kara et al. 2017, Siyal et al. 2019). The two peaks intensified in the spectra of BFA-GP indicated that hydroxyls on the surface of geopolymer increased (Siyal et al. 2019). The peak at approximately 1420 cm<sup>-1</sup> and the small one at 874 cm<sup>-1</sup> in spectrum of BFA are ascribed to asymmetric stretching and out-of-plane bending vibrations of the O—C—O bonds of CO<sub>3</sub><sup>2-</sup> (Singhal et al. 2017). The decomposition of calcium carbonate in the hydrothermal process may explain the decrease of absorption intensity at these bands. Bands near 1030 cm<sup>-1</sup> are associated with asymmetric stretching vibrations of Si—O—T (T = Si or Al) (Barbosa et al. 2018). This is the principal band used to recognize the synthesis of geopolymers (Siyal et al. 2019) and is well characterized in the literature (Siyal et al. 2019, Wang et al. 2020, Tian, Nakama and Sasaki 2019). This peak deepened obviously after modification, indicating there are significant amount of geopolymer in BFA-GP. Here, Al—O is longer and weaker than Si—O, and the shift of the peak to lower

wavenumbers (from 1033 cm<sup>-1</sup> for BFA to 1000 cm<sup>-1</sup> for BFA-GP) indicates that the degree of silicon substitution by aluminum increased. The bands at 777 cm<sup>-1</sup> corresponded to the cyclosilicate vibrations which is a kind of silica tetrahedron oligomer (Acisli, Acar and Khataee 2020, Lecomte et al. 2006) this is other evidence of rearrangement of aluminosilicate (He et al. 2020, Huang and Han 2011).

The spectrum of BFA-GP-Cd in Fig. 6 (a) show that the absorption of —OH at 3440 cm<sup>-1</sup> decreased compared to BFA-GP suggesting that coordination reaction likely occurred between Cd<sup>2+</sup> and surface hydroxyl group. Meanwhile, the peak of Si—O—T (T = Si or Al) shift to higher wavenumbers after adsorption, indicating Si—O—T (T = Si or Al) group also adsorbed significant amount of Cd<sup>2+</sup>.

The XPS spectra provided molecular structure information of the BFA and BFA-GP as shown in Fig. 6. The intensity of peaks corresponding to Si, O, Al, and Ca elements changed indicating the transformation of chemical bond during the modification. The intensification of O, Si, and Al peaks mainly due to the polymerization of aluminosilicate. Formation of gismondine (CaAl<sub>2</sub>Si<sub>2</sub>O<sub>8</sub>·4H<sub>2</sub>O) may explain the peak intensification corresponding to calcium. There are three types of primary chemical states of oxygen in geopolymer including Si—O—Al, Si—O—Si, and Si—O—H with the main absorption signal positions at 531, 532, and 533 eV according to the literature (Simonsen et al. 2009, Jhang, Boscoboinik and Altman 2020). The fitted parameters of the O1 s XPS spectra are shown in Fig. 4(e) and (f) for BFA and BFA-GP, respectively. There are more Si—O—Al and Si—O—H in BFA-GP, which is in accordance with the FTIR results. These results reconfirmed that new composition such as geopolymer and gismondine were formed.

### 3.1.4. Zeta potential and zero charge point

The zeta potential graphs (Fig. 7) at solution pH range of 1–9 reveal that the point of zero charge (pHPZC) of BFA-GP is at 1.3, where the adsorbent surface is having electron neutrality (Gao et al. 2015). The result clearly suggest that BFA-GP exhibited negatively charge under pH > 1.3, and Zeta poten-

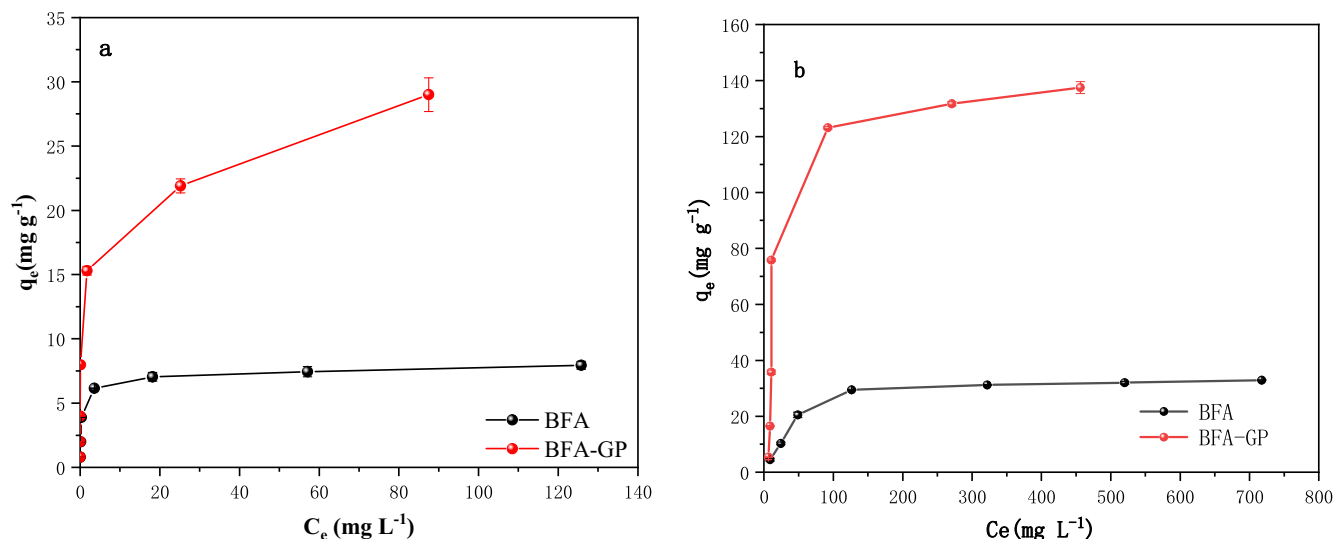


**Fig. 8** Adsorption isotherm of Cd<sup>2+</sup> (a) and Pb<sup>2+</sup> (b) on BFA-GP and BFA.

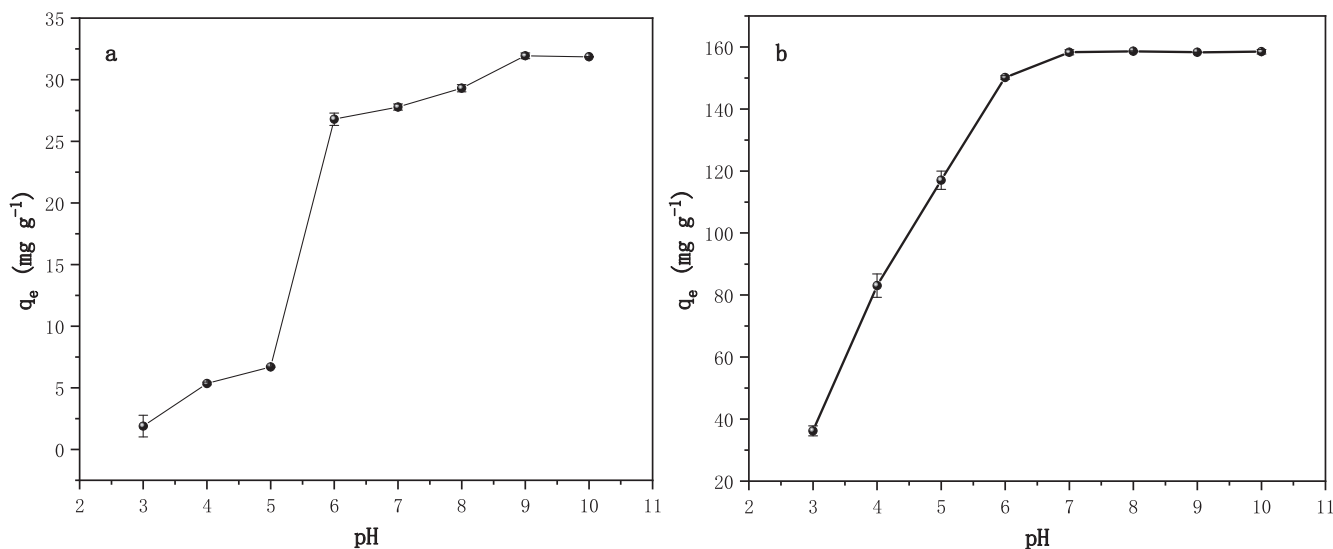


Fig. 9 Effect of initial pH on Cd<sup>2+</sup> (a) and Pb<sup>2+</sup> (b) adsorption.

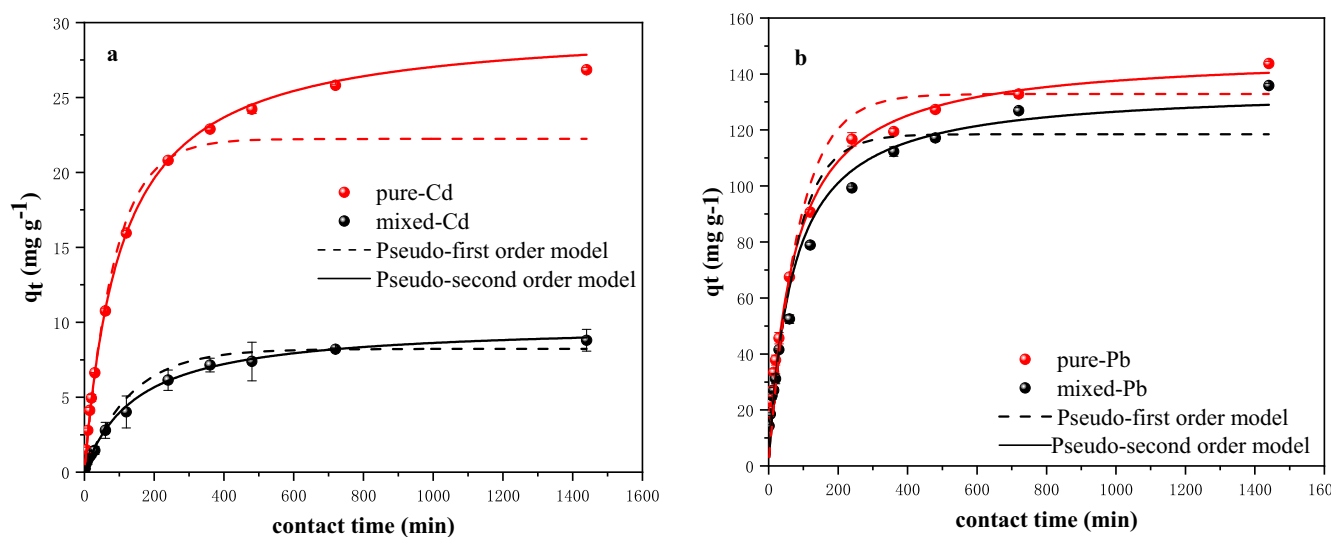


Fig. 10 Adsorption kinetics of Cd<sup>2+</sup> (a) and Pb<sup>2+</sup> (b) onto BFA-GP in the pure and mixed metal system.

tial is lower than  $-23$  mV when the pH of solution higher than 3. This property is important for geopolymer to generate electrostatic attraction for the metal cations.

### 3.2. Comparison of Cd<sup>2+</sup> adsorption on BFA-GP and BFA

Fig. 8 shows the adsorption amount of Cd<sup>2+</sup> and Pb<sup>2+</sup> by BFA and BFA-GP. The maximum adsorption amount of Cd<sup>2+</sup> and Pb<sup>2+</sup> increased from 7.94 to 29.92 mg g<sup>-1</sup> and 32.87 to 137.49 mg g<sup>-1</sup> respectively after modification, indicating BFA-GP synthesized is a high efficiency adsorbent for heavy metal ions.

### 3.3. Effect of pH

The pH value of the aqueous solution affects both the surface charges of adsorbent and the degree of ionization of heavy

metal ion, so it is an important variable to adsorption effect (Bao et al. 2013). The Fig. 9 illustrated the adsorption amounts of metal ions at different pH conditions. The sorption ability of BFA-GP for heavy metals increased rapidly with the increasing of solution pH. The adsorption amounts of Pb<sup>2+</sup> increased at pH between 3 and 6, and amount adsorbed was near constant after pH 6. With regard to Cd<sup>2+</sup>, the adsorption amounts were very low when pH was below 5, and increased quickly between pH 5 and 6, after pH 6 adsorption amounts increased slowly and reached equilibrium gradually. This results may be related to the surface charge of BFA-GP. At low pH, higher concentration of H<sup>+</sup> present in the reaction solutions, which can compete with heavy metal ions for the adsorption sites, and the functional groups of adsorbent were protonated, significant electrostatic repulsion exists between positively charge surface and heavy metal ions. With the increasing of solution pH, the concentration of the H<sup>+</sup> decreases and deprotonation would occur on the surface of

**Table 2** Kinetic model parameters using Pseudo-first order model and Pseudo-second order model for Cd<sup>2+</sup> and Pb<sup>2+</sup> adsorption by BFA-GP in their pure and mixed solution.

Solution	$q_{ee}$ (mg g <sup>-1</sup> )	Pseudo-first order model			Pseudo-second order model		
		$q_e$ (mg g <sup>-1</sup> )	$k_1$ (min <sup>-1</sup> )	$R^2$	$q_e$ (mg g <sup>-1</sup> )	$k_2$ (g mg <sup>-1</sup> min <sup>-1</sup> ) ( $\times 10^4$ )	$R^2$
Pure-Cd	26.84	22.23	0.0117	0.9979	29.88	3.19	0.9999
Mixed-Cd	8.8	8.22	0.0076	0.9988	9.91	6.71	0.9996
Pure-Pb	143.73	132.85	0.0118	0.9349	147.36	0.96	0.9840
Mixed-Pb	136.93	118.48	0.0136	0.9608	135.04	1.10	0.9695

$q_{ee}$  is the experimental value,  $q_e$  is the equilibrium adsorption capacity calculated by Pseudo-first order model and Pseudo-second order model.

BFA-GP, the surface negative charge increased, which enhanced the adsorption of positively charged metal cations by electrostatic attraction. Similar theories have also been proposed by other researchers for the metal adsorption (Liu and Zhang 2009, Duan and Su 2014, Huang et al. 2020b, Liu et al. 2016). Additionally, adsorption amounts of Cd<sup>2+</sup> and Pb<sup>2+</sup> reach constant at different pH maybe due to the different hydrolysis precipitation property of two ions (Xu 2008). Considering the large amount of precipitation of metal ions could affect the adsorption under high pH, selecting pH = 6.5 as the optimum condition for subsequent experiments.

### 3.4. Characterization of adsorption kinetics

Fig. 10 shows the kinetic adsorption curves of Cd<sup>2+</sup> and Pb<sup>2+</sup> on BFA-GP in pure and mixed solutions. The adsorption process of Cd<sup>2+</sup> and Pb<sup>2+</sup> by BFA-GP shows two different stages. The first stage is fast and should be adsorption on the surface and the second stage is slow adsorption and due to the diffusion to narrow cracks and pores (Qiu, Cheng and Huang 2018). At initial stage of the reaction, there are a large number of vacant adsorption sites on the adsorbent surface, and the heavy metal ions diffusing to the adsorbent surface can be captured by the adsorption sites quickly; on the other hand, the abundant Cd<sup>2+</sup> and Pb<sup>2+</sup> in the solution enhance mass transfer driving force in the liquid phase, which is beneficial to the diffusion of metal ions to the adsorbent surface. The adsorption rate slowed down after 240 min indicating that the adsorption sites on the adsorbent surface were saturated, the Cd<sup>2+</sup> and Pb<sup>2+</sup> began to diffuse to narrow pores in the BA-GP. At adsorption equilibrium, the adsorption quantity of Cd<sup>2+</sup> and Pb<sup>2+</sup> in pure solution was 26.84 and 143.73 mg g<sup>-1</sup>, respectively. The adsorption capacity in a mixed Cd<sup>2+</sup> and Pb<sup>2+</sup> solution was 8.80 and 135.88 mg g<sup>-1</sup>, this is 67.2% and 5.4% lower than their adsorption in pure solution.

To further investigation mechanisms of adsorption, pseudo-first-order kinetics model, pseudo-second-order kinetics model and intra-particle diffusion model have been used to evaluate the kinetics data both in pure and mixed solution.

Pseudo-first-order kinetics model often express the adsorption process in which the reaction rate is controlled by physical diffusion (Eq. (2)). Pseudo-second-order kinetics model is used to describe chemisorption exists between the adsorbate and the adsorbents (Eq. (3)). The intra-particle diffusion model is employed to decide if intra particle diffusion is the only rate limiting step in the adsorption process (Eq. (4)) (Zhu et al. 2017).

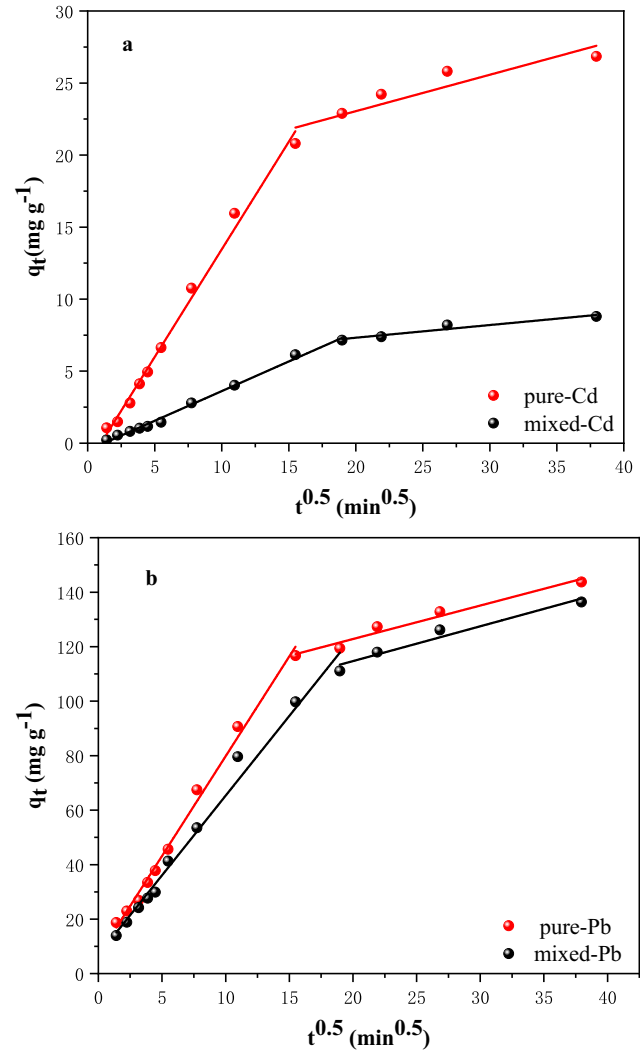


**Fig. 11** Intra-particle diffusion model plots of Cd<sup>2+</sup> (a) and Pb<sup>2+</sup> (b) in pure and mixed solution.

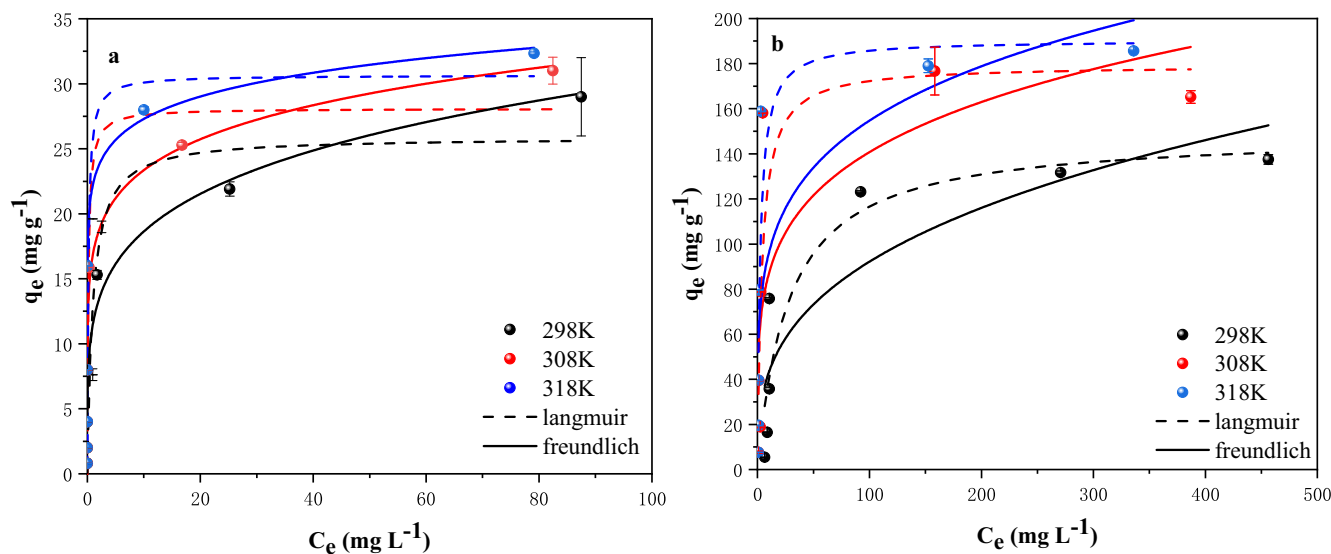
$$q_t = q_e(1 - e^{-k_1 t}) \quad (2)$$

$$q_t = \frac{k_2 q_e^2 t}{1 + k_2 q_e t} \quad (3)$$

$$q_t = k_{ip} t^{0.5} + C \quad (4)$$

**Table 3** Kinetic parameters using intra-particle diffusion model for the adsorption of  $\text{Cd}^{2+}$  and  $\text{Pb}^{2+}$  adsorption by BFA-GP in the pure and mixed solution.

Solution	Stage1		Stage2	
	$k_{ip-1}$ ( $\text{mg g}^{-1} \text{min}^{-0.5}$ )	$R^2$	$k_{ip-2}$ ( $\text{mg g}^{-1} \text{min}^{-0.5}$ )	$R^2$
Pure-Cd	1.493	0.9921	0.253	0.8545
Mixed-Cd	0.412	0.9950	0.088	0.9372
Pure-Pb	7.327	0.9933	1.229	0.9858
Mixed-Pb	5.851	0.9863	1.278	0.9589

**Fig. 12** Adsorption isotherms of  $\text{Cd}^{2+}$  (a) and  $\text{Pb}^{2+}$  (b) at different temperature in pure systems.**Table 4** Isotherm model parameters for  $\text{Cd}^{2+}$  and  $\text{Pb}^{2+}$  adsorption by BFA-GP in their pure solution.

Metal	T/K	$q_{ee}$	Langmuir			Freundlich		
			$k_l$ ( $\text{L mg}^{-1}$ )	$q_m$ ( $\text{mg L}^{-1}$ )	$R^2$	$k_f$	n	$R^2$
Cd	298	29.92	1.0281	25.89	0.8794	11.5502	4.8099	0.9721
	308	31.01	5.5461	28.10	0.9175	16.9278	7.1505	0.9691
	318	32.34	5.3649	30.66	0.7001	22.2795	11.3308	0.9131
Pb	298	137.49	0.0359	149.01	0.8846	19.9510	3.0096	0.789
	308	165.20	0.2441	179.30	0.7799	53.1437	4.7288	0.6112
	318	185.62	0.3936	190.39	0.8053	59.1397	4.7893	0.6582

$q_{ee}$  is the experimental value.

where  $q_e$  ( $\text{mg g}^{-1}$ ) and  $q_t$  ( $\text{mg g}^{-1}$ ) are the uptake amounts of the metal ions adsorbed on the BFA-GP at equilibrium and at any time (t).  $k_1$  ( $\text{min}^{-1}$ ) and  $k_2$  ( $\text{g} \cdot \text{mg}^{-1} \cdot \text{min}^{-1}$ ) are the adsorption rate constants of the pseudo-first order and pseudo-second order models, respectively.  $k_{ip}$  is the intra-particle diffusion rate constant, and C ( $\text{mg g}^{-1}$ ) is the constant related to the extent of boundary layer thickness.

The fitting results of pseudo-first-order and pseudo-second-order kinetics model are illustrated in Fig. 10, and the kinetic parameters are presented in Table 2. The correlation coefficient

of pseudo-second-order kinetics model is higher than that of the pseudo-first-order model, the equilibrium adsorption capacity calculated by the pseudo-second-order kinetic model is closer to the experimental values in all the cases. The results show that the adsorption process of  $\text{Cd}^{2+}$  and  $\text{Pb}^{2+}$  onto BFA-GP in pure and mixed solutions is more consistent with the pseudo-second-order kinetics model, indicating chemisorption is the predominant step of the adsorption process (Gao et al. 2015). This was also found in other studies (Wang, Terdkiatburana and Tadé 2008).

Adsorbents	Adsorptive capacity (mg g <sup>-1</sup> )		References
	Cd	Pb	
BFA and slags-based geopolymers	10.58	50	(Pérez-Villarejo et al. 2018)
Alkali-activated fly ash	26.47	–	(Krol et al. 2018)
Zeolite-based geopolymer	26.25	–	(Javadian, 2013)
Geopolymer-alginate-chitosan composites	–	142.67	(Yan et al. 2019)
Biofuel ash based geopolymer	29.92	137.49	This study

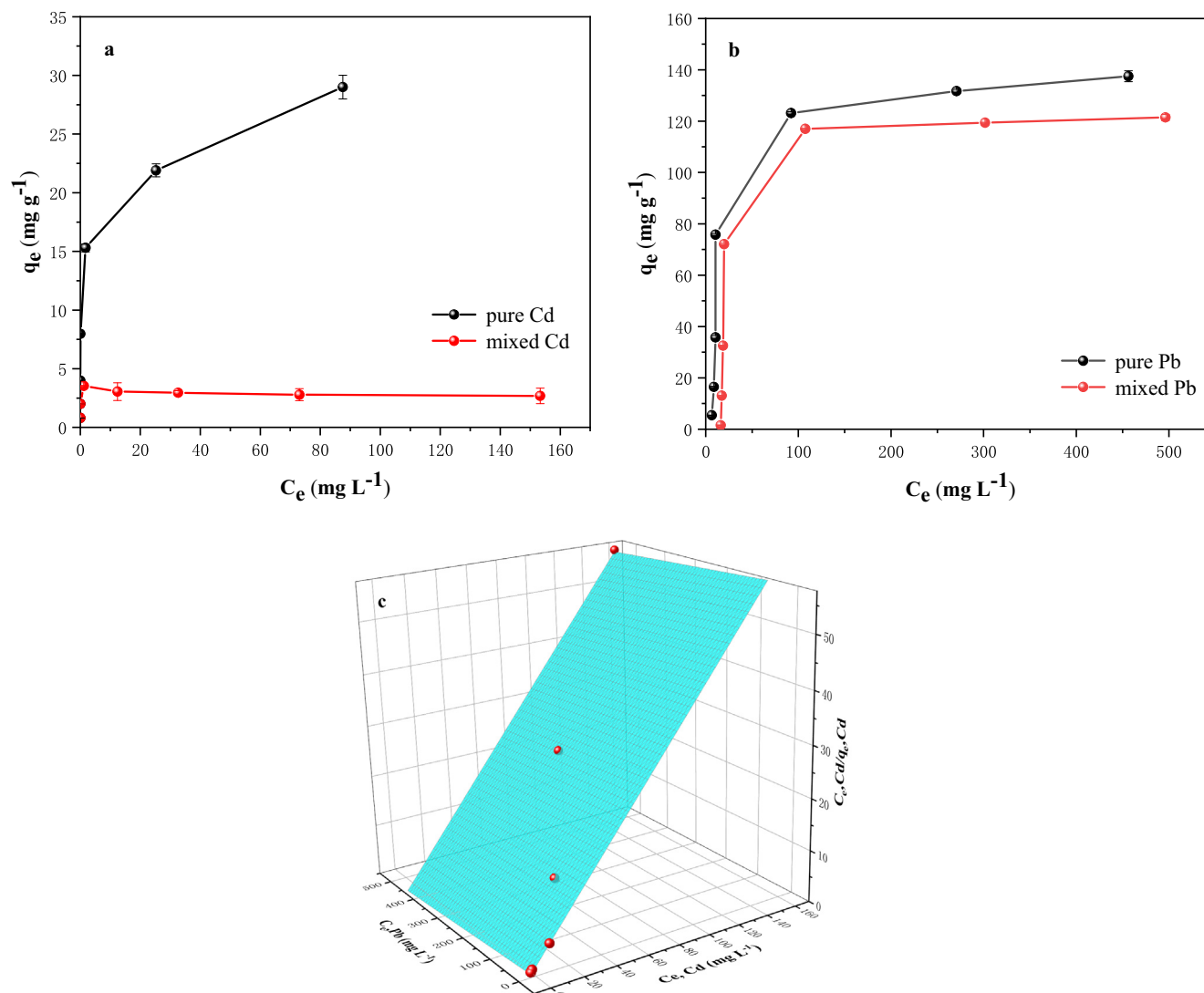


**Fig. 13** Comparison of adsorption quantity of Cd<sup>2+</sup> (a) and Pb<sup>2+</sup> (b) in pure and mixed solution and Langmuir competitive adsorption model for Cd<sup>2+</sup> and Pb<sup>2+</sup> adsorption on BFA-GP (c).

It is generally believed that the adsorption process can be divided into three steps: i) external diffusion—heavy metal ions diffuse onto the external surface of the adsorbent, ii) internal diffusion—adsorbates diffuse into the pore channels of the adsorbent, and iii) the reaction of adsorbates and adsorption

sites external or internal of the adsorbent. The rate of reaction is usually fast, and thus the first two processes are the factors controlling adsorption rate. The intra-particle diffusion model is suitable to describe the kinetics in which the diffusion inside the particle is dominated. If the curve of  $q_t$  versus  $t^{0.5}$  is a

straight line and passes through the origin, then this indicates that the intra-particle diffusion process is the only rate-limiting step to control the adsorption rate (Kong et al. 2016).

Fig. 11 shows the fitting line segments of the intraparticle diffusion model for the experimental data and the fitting parameters are laid out in Table 3. The curves did not pass through origin, and the experimental data showed multiple linear relationships indicating that the adsorption of  $\text{Cd}^{2+}$  and  $\text{Pb}^{2+}$  onto BFA-GP is controlled by two or more factors. The experimental data plot can be fitted as two linear stages: i) 0–240 min with a fast reaction rate that is the external diffusion process; ii) a slow adsorption stage controlled by the internal diffusion process of  $\text{Cd}^{2+}$  and  $\text{Pb}^{2+}$ .

### 3.5. Adsorption isotherms of $\text{Cd}^{2+}$ and $\text{Pb}^{2+}$ on BFA-GP

#### 3.5.1. Adsorption isotherms in pure solution

Both Langmuir model (Eq. (5)) and Freundlich model (Eq. (6)) was used to fit the adsorption isotherms:

$$q_e = \frac{q_m k_f C_e}{1 + k_f} \quad (5)$$

where  $q_e$  ( $\text{mg g}^{-1}$ ) represents the equilibrium adsorption amount,  $q_m$  ( $\text{mg g}^{-1}$ ) is the maximum adsorption amount calculated by the Langmuir equation,  $k_f$  ( $\text{L mg}^{-1}$ ) is the Langmuir adsorption equilibrium constant.

$$q_e = k_f C_e^{1/n} \quad (6)$$

where  $k_f$  and  $n$  are the Freundlich equilibrium constants, which are related to the adsorption capacity and intensity of adsorption, respectively (Police et al. 2020). Values of  $n$  between 2 and 10 shows easy adsorption (Bao et al. 2013).

Nonlinear fitted curves of experimental data at different temperatures in pure solution by two adsorption isotherms are displayed in Fig. 12, the related constants are listed in Table 4. The correlation coefficients  $R^2$  show that the Freundlich isotherms can better describe the adsorption of  $\text{Cd}^{2+}$  on BFA-GP indicating the heterogeneity of the adsorbent sur-

face and multi-layer adsorption may occur (Chen et al. 2017). The  $\text{Pb}^{2+}$  adsorption on BFA-GP is more consistent with the Langmuir adsorption isotherm indicating that the adsorption process of  $\text{Pb}^{2+}$  was monolayer adsorption containing chemical reactions such as ion exchange and electron sharing (Qiu et al. 2018). Based on the data in Table 4, all the  $k_f$  values increase with increasing temperature, which indicates that high temperature benefits adsorption of  $\text{Cd}^{2+}$  and  $\text{Pb}^{2+}$  by BFA-GP. The values of  $n$  are always greater than 2 at different temperatures for both  $\text{Cd}^{2+}$  and  $\text{Pb}^{2+}$ . This shows the high adsorption intensity between adsorbate and adsorbent.

Comparison of the maximum adsorption capacities of BFA-GP for  $\text{Cd}^{2+}$  and  $\text{Pb}^{2+}$  with other similar adsorbents reported in literatures are listed in Table 5. Clearly, the BFA-GP produced in this study shown a higher or equivalent adsorption capacity for  $\text{Cd}^{2+}$  and  $\text{Pb}^{2+}$  compare with most of the similar adsorbents.

#### 3.5.2. Competitive adsorption

The competitive adsorption of heavy metals by BFA-GP was shown in Fig. 13 (a) and (b). When the concentrations of  $\text{Cd}^{2+}$  and  $\text{Pb}^{2+}$  in the solution are below 20 and 100  $\text{mg L}^{-1}$ , respectively, the adsorption of  $\text{Cd}^{2+}$  and  $\text{Pb}^{2+}$  in mixed solution is consistent with adsorption in pure solution indicating that competitive adsorption is not significant at low concentrations. This is because BFA-GP can provide sufficient adsorption sites in low concentration solutions. If the concentration of the two ions in the solution is higher than 20 and 100  $\text{mg L}^{-1}$ , then the adsorption amount of two ions in mixed solution was lower than that in pure solutions.

The adsorption amount of  $\text{Cd}^{2+}$  in mixed solution is obviously lower than in pure solution, but the adsorption amount of  $\text{Pb}^{2+}$  has no significant changes indicating that the presence of  $\text{Pb}^{2+}$  seriously limits the adsorption of  $\text{Cd}^{2+}$ . Similar results were shown in previous literature (Ma et al. 2015, Cheng et al. 2012, Huang et al. 2020a). Smaller hydration ion radius, smaller surface free energy and stronger adsorption affinity lead to easier adsorption (Chen et al. 2019b). The hydrated ionic radius of lead (4.01 Å) is smaller than that of cadmium (4.26 Å), and thus  $\text{Pb}^{2+}$  enters the micro-pore of the adsorbent more easily. The surface free energy of  $\text{Cd}^{2+}$  and  $\text{Pb}^{2+}$  hydrated ions is 4.26 and 4.01  $\text{kcal mol}^{-1}$ , respectively. A larger free energy keeps  $\text{Cd}^{2+}$  in solution. The affinity depends on their hydrolysis constant  $K$ , and the ions with a large hydrolysis constant are more prone to forming metal hydroxy groups (e.g.,  $\text{Pb}(\text{OH})^-$  and  $\text{Cd}(\text{OH})^-$ ) in the solution. The  $\text{pK}$  values of  $\text{Pb}^{2+}$  and  $\text{Cd}^{2+}$  are 7.7 and 10.1, respectively. In other words, the hydrolysis constant of  $\text{Pb}^{2+}$  is about 250-fold that of  $\text{Cd}^{2+}$ , which determines that the adsorption affinity order is  $\text{Pb}^{2+} > \text{Cd}^{2+}$ .

Langmuir competitive adsorption model was introduced to fit the adsorption data obtained in mixed solution. Langmuir competitive adsorption model can be expressed as follow (Huang et al. 2020b):

$$\frac{C_{e,1}}{q_{e,1}} = \frac{1}{q_{\max,1} k_{l,1}} + \frac{1}{q_{\max,1}} C_{e,1} + \frac{k_{l,2}}{q_{\max,1} k_{l,1}} C_{e,2} \quad (8)$$

where  $C_{e,i}$  ( $\text{mg L}^{-1}$ ) refers to heavy metal equilibrium concentrations,  $q_{e,i}$  ( $\text{mg g}^{-1}$ ) stand for equilibrium adsorption quantity of heavy metal,  $k_{l,i}$  ( $\text{mg L}^{-1}$ ) represent the adsorption coefficient, indicating the sorption affinity.

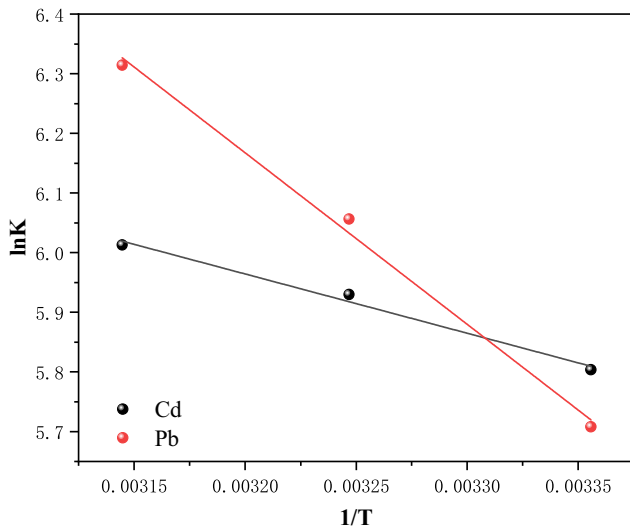


Fig. 14 Plot of  $\ln K$  against  $1/T$  obtained for the adsorption of  $\text{Cd}^{2+}$  and  $\text{Pb}^{2+}$  onto BFA-GP.

The Langmuir model fitting for the mixed system is shown in Fig. 13 (c). According to the competitive model fitting results, the correlation coefficients of Cd<sup>2+</sup> and Pb<sup>2+</sup> were 0.9995 and 0.9947, respectively, indicating that adsorption behaviors could be nicely fitted with a Langmuir competitive model.  $q_{\max}$  of Cd<sup>2+</sup> and Pb<sup>2+</sup> calculated by Langmuir model was 2.58 and 126.10 mg g<sup>-1</sup>. The fitting results are very consistent with the experimental data. This result indicates that adsorption of heavy metal ions onto BFA-GP will be restricted by other coexisting ions.

### 3.6. Adsorption thermodynamics of Cd<sup>2+</sup> and Pb<sup>2+</sup> on BFA-GP

The effect of temperature on adsorption of Cd<sup>2+</sup> and Pb<sup>2+</sup> onto BFA-GP is shown in Fig. 14. The experiments were conducted at 298, 308, and 318 K. The distribution coefficient values (K) increased with increasing temperature indicating the endothermic nature of the adsorption.

Thermodynamic parameter, free energy change ( $\Delta G$ ), enthalpy change ( $\Delta H$ ) and entropy change ( $\Delta S$ ) were calculated using Van't Hoff equation (Gao et al. 2015).

$$\Delta G = \Delta H - T\Delta S \quad (9)$$

$$\Delta G = -RT\ln K \quad (10)$$

$$\ln K = -\frac{\Delta H}{RT} + \frac{\Delta S}{R} \quad (11)$$

$$K = \frac{q_e}{C_e} \quad (12)$$

where R is gas constant (KJ mol<sup>-1</sup> K<sup>-1</sup>), T is absolute temperature (K), K is the distribution coefficient (cm<sup>3</sup> g<sup>-1</sup>) which defined as the ratio of concentration of adsorbate to adsorbent in equilibrium solution. Enthalpy change ( $\Delta H$ ) and entropy change ( $\Delta S$ ) can be obtained from slopes and intercepts of lnK versus 1/T plots.

Thermodynamic parameters of adsorption Cd<sup>2+</sup> and Pb<sup>2+</sup> on BFA-GP are listed in Table 6.  $\Delta H$  values are positive confirming that BFA-GP adsorption for Cd<sup>2+</sup> and Pb<sup>2+</sup> is endothermic (Chatterjee, Basu and Jana 2019), means a high temperature is favorable for the reaction. This is consistent with the increase of heavy metal ion adsorbing onto the BFA-GP with the increasing of temperature, as shown in Fig. 9. Although there is no clear criterion defining the adsorption type on the basis of  $\Delta H$ , the adsorption process with  $\Delta H$  ranges from 20.9 to 418.4 kJ mol<sup>-1</sup> and is recognized as a chemisorption process (Nuri and Ersoz, 2019). The enthalpy change of Cd<sup>2+</sup> and Pb<sup>2+</sup> is 8.262 and 23.912 kJ mol<sup>-1</sup>, respectively. This confirmed that chemisorption is involved in the adsorption process of Pb<sup>2+</sup>. The  $\Delta G$  values are negative indicating that the adsorption reaction is spontaneous. The entropy change ( $\Delta S$ ) is negative, which indicates that the confusion degree of the system is reduced after the adsorption reaction, and the metal ions in the solution are fixed on the surface of the adsorbent.

### 3.7. Mechanism of Cd<sup>2+</sup> and Pb<sup>2+</sup> adsorption on BFA-GP

Fig. 15 displays the SEM images and elemental mapping images of BFA-GP after adsorption Cd<sup>2+</sup> and Pb<sup>2+</sup>. The adsorption of heavy metal ions on BFA-GP was confirmed

**Table 6** Adsorption thermodynamic parameter.

Metal	$\Delta G$ (kJ mol <sup>-1</sup> )			$\Delta H$ (kJ mol <sup>-1</sup> )	$\Delta S$ (kJ mol <sup>-1</sup> T <sup>-1</sup> )
	298	308	318		
Cd	-14.379	-15.185	-15.898	8.262	-0.07603
Pb	-14.142	-15.509	-16.694	23.912	-0.12779

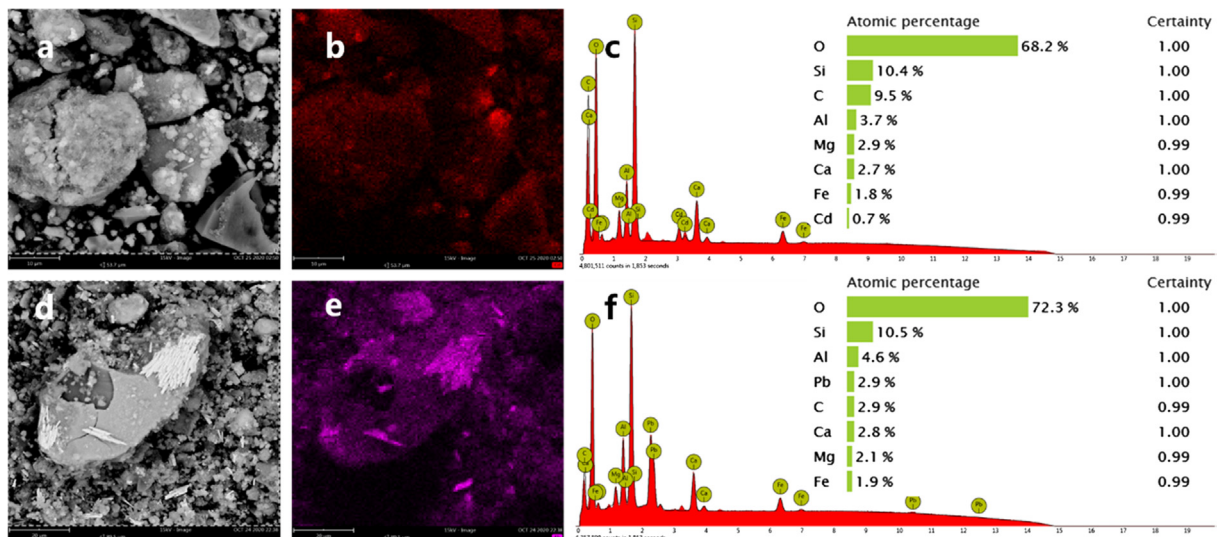


**Fig. 15** SEM-EDS analysis of BFA-GP loaded with Cd<sup>2+</sup> (a, b, c) and Pb<sup>2+</sup> (d, e, f).

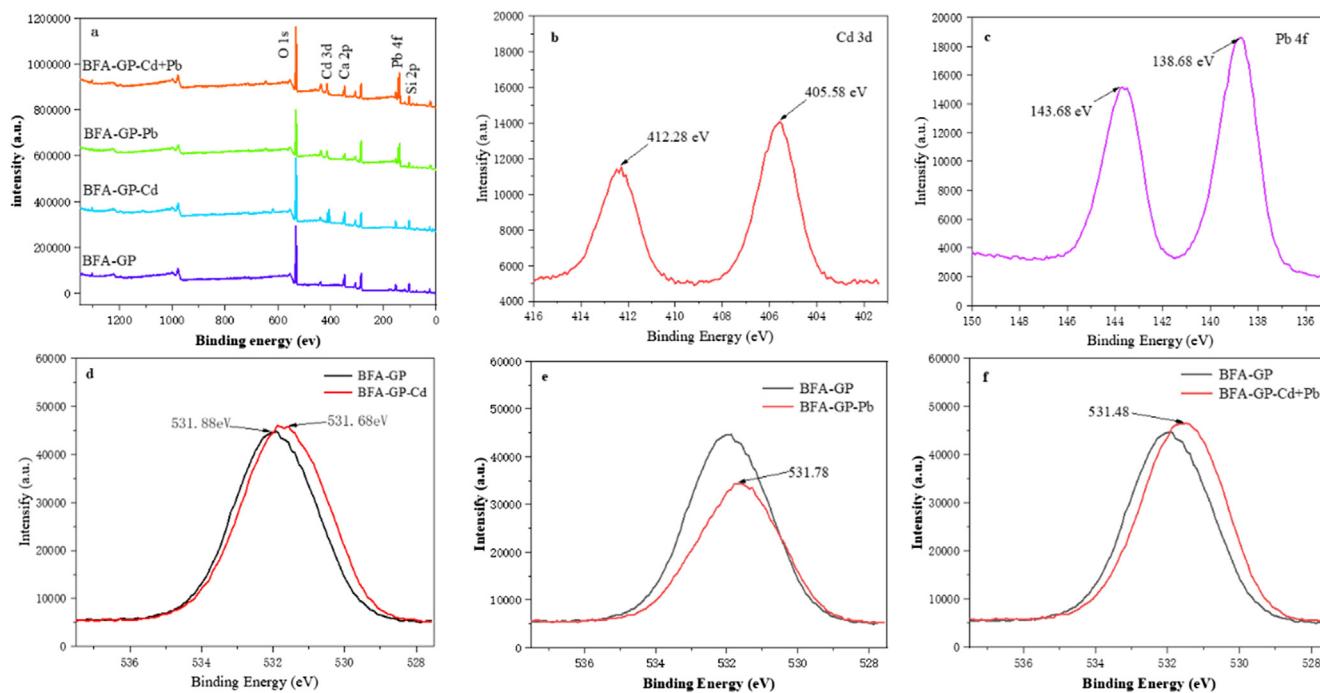


**Fig. 16** XPS spectra of BFA-GP before and after loading  $\text{Cd}^{2+}$  and  $\text{Pb}^{2+}$  in pure and mixed solution: (a) survey spectra, (b) Cd 3d spectra, (c) Pb 4f spectra, (d) O1s spectra of BFA-GP-Cd, (e) O1s spectra of BFA-GP-Pb, (f) O1s spectra of BFA-GP-Cd + Pb.

by EDS analysis. The characteristic signals of cadmium and lead elements are observed in Fig. 12 (c) and (f), respectively. In Fig. 15(a), amorphous geopolymer can be seen as white cloud-like particles on the surface of BFA-GP, and Cd can be observed predominantly adsorb on the surface of those geopolymer particles. In Fig. 15(d), needle like gismondine particles can be clearly observed, and Pb also predominantly adsorbed by gismondine particles as shown in Fig. 15(e). This clearly indicated the newly produced geopolymer and gismondine promoted the adsorption for Pb and Cd by BFA.

Fig. 16 shows the bond energy absorption analysis of BFA-GP before and after adsorption of  $\text{Cd}^{2+}$  ions and  $\text{Pb}^{2+}$  ions. The adsorption of  $\text{Cd}^{2+}$  and  $\text{Pb}^{2+}$  onto BFA-GP were also observed by the XPS spectrum. The characteristic signals of cadmium or lead elements are not observed in the spectra of BFA-GP, but appeared in the spectra of BFA-GP samples after adsorption. The bond energy absorption positions for Cd 3d are 405.58 and 412.28 eV corresponding to Cd  $3d_{5/2}$  and Cd  $3d_{3/2}$ , respectively. The bond energy absorption positions for Pb 4f are 138.68 and 143.68 eV representing Pb  $4f_{7/2}$  and Pb  $4f_{5/2}$ , respectively (Huang et al. 2020a). Moreover, Fig. 16 (d,e,f) showed that the binding energy peaks of O1s move from 531.88 to 531.68, 531.78, and 531.48 eV after adsorption of Cd, Pb, and Cd + Pb, respectively, it may be due to that the chelate reaction between heavy metal ions and oxygen containing functional groups including Si—O—Si, Si—O—Al, and Si—O—H changed the bonding energy of O1s (Kaewmee et al. 2020). The reduction in the bond strengths of Ca 2p after adsorption clearly indicated that ion-exchange occurred between heavy metal ions and  $\text{Ca}^{2+}$  in Ca—A—Si—H gel (Qiu et al. 2018). Hence, the mechanisms of the adsorption process should include electrostatic attraction, chelate reaction, and ion-exchange.

#### 4. Conclusion

A hydrothermal alkali modification method to produce geopolymer from biofuel ash at low temperature was proposed. This process partly change quartz, margarite and  $\text{CaCO}_3$  to geopolymer and Gismondine. Specific surface area and pore volume of biofuel ash was increased from  $20.41 \text{ m}^2 \text{ g}^{-1}$  and  $0.0337 \text{ cm}^3 \text{ g}^{-1}$  to  $56.63 \text{ m}^2 \text{ g}^{-1}$  and  $0.1600 \text{ cm}^3 \text{ g}^{-1}$ , respectively after the modification. The adsorption capacity of the modified biofuel ash for  $\text{Cd}^{2+}$  and  $\text{Pb}^{2+}$  can reach 29.92 and  $143.73 \text{ mg g}^{-1}$ , respectively, which is better than most similar adsorbents. Meanwhile, the binding affinity of two cations on BFA-GP followed the order of  $\text{Pb}^{2+} > \text{Cd}^{2+}$ . Kinetic experimental data are more consistent with pseudo-second-order kinetic models. Both FTIR, XPS and adsorption thermodynamics indicated the adsorption of  $\text{Cd}^{2+}$  and  $\text{Pb}^{2+}$  on BFA-GP is mainly chemical sorption, including electrostatic attraction, chelate reaction, and ion-exchange happened during the adsorption. The produced geopolymer could be used as low-cost adsorbent for heavy metal removal from wastewater, and provided a new method for the use of biomass power plant ash.

#### Funding

This study was supported by Key Research & Development Project of Hebei Province, China (Grant No.18274232), National Key Research and Development Program of China (Grant No.2019YFC1805300) and Key Research & Development Project of Guangxi Province, China (Grant No.AB17195036), Basic scientific research operating expenses of universities of Hebei Province (Grant No. QN202119). We also thank LetPub

([www.letpub.com](http://www.letpub.com)) for its linguistic assistance during the preparation of this manuscript.

### Declaration of Competing Interest

The authors declare that they have no known competing financial interests or personal relationships that could have appeared to influence the work reported in this paper.

### References

- Acisli, O., Acar, I., Khataee, A., 2020. Preparation of a fly ash-based geopolymer for removal of a cationic dye: Isothermal, kinetic and thermodynamic studies. *J. Ind. Eng. Chem.* 83, 53–63.
- Alinnor, I.J., 2007. Adsorption of heavy metal ions from aqueous solution by fly ash. *Fuel* 86, 853–857.
- Bai, C., Wang, L., Zhu, Z., 2020. Adsorption of Cr(III) and Pb(II) by graphene oxide/alginate hydrogel membrane: Characterization, adsorption kinetics, isotherm and thermodynamics studies. *Int. J. Biol. Macromol.* 147, 898–910.
- Bao, W.-W., Zou, H.-F., Gan, S.-C., Xu, X.-C., Ji, G.-J., Zheng, K.-Y., 2013. Adsorption of heavy metal ions from aqueous solutions by zeolite based on oil shale ash: Kinetic and equilibrium studies. *Chem. Res. Chin. Univ.* 29, 126–131.
- Barbosa, T.R., Foletto, E.L., Do tto, G.L., Jahn, S.L., 2018. Preparation of mesoporous geopolymer using metakaolin and rice husk ash as synthesis precursors and its use as potential adsorbent to remove organic dye from aqueous solutions. *Ceram. Int.* 44, 416–423.
- Chatterjee, A., Basu, J.K., Jana, A.K., 2019. Alumina-silica nanosorbent from plant fly ash and scrap aluminium foil in removing nickel through adsorption. *Powder Technol.* 354, 792–803.
- Chen, F., Wang, K., Shao, L., Muhammad, Y., Wei, Y., Gao, F., Wang, X., Cui, X., 2019a. Synthesis of Fe<sub>2</sub>O<sub>3</sub>-modified porous geopolymer microspheres for highly selective adsorption and solidification of F<sup>-</sup> from waste-water. *Compos. Part B: Eng.*, 178.
- Chen, G., Shah, K.J., Shi, L., Chiang, P.-C., 2017. Removal of Cd(II) and Pb(II) ions from aqueous solutions by synthetic mineral adsorbent: Performance and mechanisms. *Appl. Surf. Sci.* 409, 296–305.
- Chen, X., Guo, Y., Ding, S., Zhang, H., Xia, F., Wang, J., Zhou, M., 2019b. Utilization of red mud in geopolymer-based pervious concrete with function of adsorption of heavy metal ions. *J. Cleaner Prod.* 207, 789–800.
- Cheng, T.W., Lee, M.L., Ko, M.S., Ueng, T.H., Yang, S.F., 2012. The heavy metal adsorption characteristics on metakaolin-based geopolymer. *Appl. Clay Sci.* 56, 90–96.
- Darmayanti, L., Kadja, G.T.M., Notodarmojo, S., Damanhuri, E., Mukti, R.R., 2019. Structural alteration within fly ash-based geopolymers governing the adsorption of Cu(2+) from aqueous environment: Effect of alkali activation. *J. Hazard Mater.* 377, 305–314.
- Di Natale, F., Gargiulo, V., Alfe, M., 2020. Adsorption of heavy metals on silica-supported hydrophilic carbonaceous nanoparticles (SHNPs). *J. Hazard Mater.* 393, 122374.
- Duan, J., Su, B., 2014. Removal characteristics of Cd(II) from acidic aqueous solution by modified steel-making slag. *Chem. Eng. J.* 246, 160–167.
- Duarte-Nass, C., Rebolledo, K., Valenzuela, T., Kopp, M., Jeison, D., Rivas, M., Azocar, L., Torres-Aravena, A., Ciudad, G., 2020. Application of microbe-induced carbonate precipitation for copper removal from copper-enriched waters: Challenges to future industrial application. *J. Environ. Manage.* 256, 109938.
- Fakhre, N.A., Ibrahim, B.M., 2018. The use of new chemically modified cellulose for heavy metal ion adsorption. *J. Hazard Mater.* 343, 324–331.
- Gao, M., Ma, Q., Lin, Q., Chang, J., Bao, W., Ma, H., 2015. Combined modification of fly ash with Ca(OH)<sub>2</sub>/Na<sub>2</sub>FeO<sub>4</sub> and its adsorption of Methyl orange. *Appl. Surf. Sci.* 359, 323–330.
- He, P.Y., Zhang, Y.J., Chen, H., Han, Z.C., Liu, L.C., 2020. Low-cost and facile synthesis of geopolymer-zeolite composite membrane for chromium(VI) separation from aqueous solution. *J. Hazard Mater.* 392, 122359.
- Javadian, H., 2013. Study of the adsorption of Cd (II) from aqueous solution using zeolite-based geopolymer, synthesized from Coal Fly Ash, Kinetic, isotherm and thermodynamic studies. *Arabian J. Chem.* <https://doi.org/10.1016/j.arabjch.2013.02.018>.
- Hong, M., Yu, L., Wang, Y., Zhang, J., Chen, Z., Dong, L., Zan, Q., Li, R., 2019. Heavy metal adsorption with zeolites: The role of hierarchical pore architecture. *Chem. Eng. J.* 359, 363–372.
- Huang, X., Zemlyanov, D.Y., Diaz-Amaya, S., Salehi, M., Stanciu, L., Whelton, A.J., 2020a. Competitive heavy metal adsorption onto new and aged polyethylene under various drinking water conditions. *J. Hazard Mater.* 385, 121585.
- Huang, X., Zhao, H., Zhang, G., Li, J., Yang, Y., Ji, P., 2020b. Potential of removing Cd(II) and Pb(II) from contaminated water using a newly modified fly ash. *Chemosphere* 242, 125148.
- Huang, Y., Han, M., 2011. The influence of alpha-Al<sub>2</sub>O<sub>3</sub> addition on microstructure, mechanical and formaldehyde adsorption properties of fly ash-based geopolymer products. *J. Hazard Mater.* 193, 90–94.
- Hui-Teng, N., Cheng-Yong, H., Yun-Ming, L., Abdullah, M.M.A.B., Ern Hun, K., Razi, H.M., Yong-Sing, N., 2021. Formulation, mechanical properties and phase analysis of fly ash geopolymer with ladle furnace slag replacement. *J. Mater. Res. Technol.* 12, 1212–1226.
- Jhang, J.H., Boscoboinik, J.A., Altman, E.I., 2020. Ambient pressure x-ray photoelectron spectroscopy study of water formation and adsorption under two-dimensional silica and aluminosilicate layers on Pd(111). *J. Chem. Phys.* 152, 084705.
- Jiang, H., Yang, Y., Lin, Z., Zhao, B., Wang, J., Xie, J., Zhang, A., 2020. Preparation of a novel bio-adsorbent of sodium alginate grafted polyacrylamide/graphene oxide hydrogel for the adsorption of heavy metal ion. *Sci. Total Environ.* 744, 140653.
- Kaewmee, P., Song, M., Iwanami, M., Tsutsumi, H., Takahashi, F., 2020. Porous and reusable potassium-activated geopolymer adsorbent with high compressive strength fabricated from coal fly ash wastes. *J. Cleaner Prod.* 272.
- Kara, İ., Yilmazer, D., Akar, S.T., 2017. Metakaolin based geopolymer as an effective adsorbent for adsorption of zinc(II) and nickel (II) ions from aqueous solutions. *Appl. Clay Sci.* 139, 54–63.
- Khale, D., Chaudhary, R., 2007. Mechanism of geopolymerization and factors influencing its development: a review. *J. Mater. Sci.* 42, 729–746.
- Kong, X., Han, Z., Zhang, W., Song, L., Li, H., 2016. Synthesis of zeolite-supported microscale zero-valent iron for the removal of Cr (6+) and Cd(2+) from aqueous solution. *J. Environ. Manage.* 169, 84–90.
- Krol, M., Rozek, P., Chlebda, D., Mozgawa, W., 2018. Influence of alkali metal cations/type of activator on the structure of alkali-activated fly ash - ATR-FTIR studies. *Spectrochim. Acta A Mol. Biomol. Spectrosc.* 198, 33–37.
- Lecomte, I., Henrist, C., Liégeois, M., Maseri, F., Rulmont, A., Cloots, R., 2006. (Micro)-structural comparison between geopolymers, alkali-activated slag cement and Portland cement. *J. Eur. Ceram. Soc.* 26, 3789–3797.
- Lin, Z., Li, J., Luan, Y., Dai, W., 2020. Application of algae for heavy metal adsorption: A 20-year meta-analysis. *Ecotoxicol. Environ. Saf.* 190, 110089.
- Liu, Y., Yan, C., Zhang, Z., Wang, H., Zhou, S., Zhou, W., 2016. A comparative study on fly ash, geopolymer and faujasite block for Pb removal from aqueous solution. *Fuel* 185, 181–189.

- Liu, Z., Zhang, F.S., 2009. Removal of lead from water using biochars prepared from hydrothermal liquefaction of biomass. *J. Hazard Mater.* 167, 933–939.
- Ma, X., Yang, S.T., Tang, H., Liu, Y., Wang, H., 2015. Competitive adsorption of heavy metal ions on carbon nanotubes and the desorption in simulated biofluids. *J. Colloid Interface Sci.* 448, 347–355.
- Nekouei, R.K., Pahlevani, F., Assefi, M., Maroufi, S., Sahajwalla, V., 2019. Selective isolation of heavy metals from spent electronic waste solution by macroporous ion-exchange resins. *J. Hazard Mater.* 371, 389–396.
- Novais, R.M., Carvalheiras, J., Tobaldi, D.M., Seabra, M.P., Pullar, R.C., Labrincha, J.A., 2019. Synthesis of porous biomass fly ash-based geopolymer spheres for efficient removal of methylene blue from wastewaters. *J. Cleaner Prod.* 207, 350–362.
- Nuri, Unlu, Ersoz, Mustafa, 2019. Adsorption characteristics of heavy metal ions onto a low cost biopolymeric sorbent from aqueous solutions. *J. Hazard. Mater.* B136, 272–280.
- Onutai, S., Kobayashi, T., Thavorniti, P., Jiemsirilers, S., 2019. Porous fly ash-based geopolymer composite fiber as an adsorbent for removal of heavy metal ions from wastewater. *Mater. Lett.* 236, 30–33.
- Pérez-Villarejo, L., Bonet-Martínez, E., Eliche-Quesada, D., Sánchez-Soto, P.J., Rincón-López, J.M., Castro-Galiano, E., 2018. Biomass fly ash and aluminium industry slags-based geopolymers. *Mater. Lett.* 229, 6–12.
- Police, S., Maity, S., Chaudhary, D.K., Dusane, C.K., Sahu, S.K., Kumar, A.V., 2020. Effect of coal fly ash's particle size on U adsorption in water samples and thermodynamic study on adsorption. *Environ. Chem. Ecotoxicol.* 2, 32–38.
- Qiao, L., Li, S., Li, Y., Liu, Y., Du, K., 2020. Fabrication of superporous cellulose beads via enhanced inner cross-linked linkages for high efficient adsorption of heavy metal ions. *J. Cleaner Prod.* 253.
- Qin, Z., Zhuang, Q., Cai, X., He, Y., Huang, Y., Jiang, D., Lin, E., Liu, Y., Tang, Y., Wang, M.Q., 2018. Biomass and biofuels in China: Toward bioenergy resource potentials and their impacts on the environment. *Renew. Sustain. Energy Rev.* 82, 2387–2400.
- Qiu, R., Cheng, F., Huang, H., 2018. Removal of Cd<sup>2+</sup> from aqueous solution using hydrothermally modified circulating fluidized bed fly ash resulting from coal gangue power plant. *J. Cleaner Prod.* 172, 1918–1927.
- Rasaki, S.A., Bingxue, Z., Guarecuco, R., Thomas, T., Minghui, Y., 2019. Geopolymer for use in heavy metals adsorption, and advanced oxidative processes: A critical review. *J. Cleaner Prod.* 213, 42–58.
- Rožek, P., Król, M., Mozgawa, W., 2019. Geopolymer-zeolite composites: A review. *J. Cleaner Prod.* 230, 557–579.
- Santa, R.A.A.B., Padoin, N., Soares, C., Riella, H.G., 2021. Microstructural characteristics of geopolymer materials with twenty eight days of curing and after eight years stored at room temperature. *J. Cleaner Prod.* 278.
- Sarkar, C., Basu, J.K., Samanta, A.N., 2019. Experimental and kinetic study of fluoride adsorption by Ni and Zn modified LD slag based geopolymer. *Chem. Eng. Res. Des.* 142, 165–175.
- Andrejkovičová, S., 2016. The effect of natural zeolite on microstructure, mechanical and heavy metals adsorption properties of metakaolin based geopolymers. *Appl. Clay Sci.* 126, 141–152.
- Sha, D., Pan, B., Sun, Y., 2020. A novel raw material for geopolymers: Coal-based synthetic natural gas slag. *J. Cleaner Prod.* 262.
- Shahrokhi-Shahraki, R., Benally, C., El-Din, M.G., Park, J., 2020. High efficiency removal of heavy metals using tire-derived activated carbon vs commercial activated carbon: Insights into the adsorption mechanisms. *Chemosphere* 264, 128455.
- Shao, N., Li, S., Yan, F., Su, Y., Liu, F., Zhang, Z., 2020. An all-in-one strategy for the adsorption of heavy metal ions and photodegradation of organic pollutants using steel slag-derived calcium silicate hydrate. *J. Hazard. Mater.* 382.
- Shi, R., Li, J., Jiang, J., Mehmood, K., Liu, Y., Xu, R., Qian, W., 2017. Characteristics of biomass ashes from different materials and their ameliorative effects on acid soils. *J. Environ. Sci. (China)* 55, 294–302.
- Simonsen, M.E., Sønderby, C., Li, Z., Søgaard, E.G., 2009. XPS and FT-IR investigation of silicate polymers. *J. Mater. Sci.* 44, 2079–2088.
- Singhal, A., Gangwar, B.P., Gayathry, J.M., 2017. CTAB modified large surface area nanoporous geopolymer with high adsorption capacity for copper ion removal. *Appl. Clay Sci.* 150, 106–114.
- Siyal, A.A., Azizli, K.A., Man, Z., Ismail, L., Khan, M.I., 2016. Geopolymerization kinetics of fly ash based geopolymers using JMAK model. *Ceram. Int.* 42, 15575–15584.
- Siyal, A.A., Shamsuddin, M.R., Khan, M.I., Rabat, N.E., Zulfikar, M., Man, Z., Siame, J., Azizli, K.A., 2018. A review on geopolymers as emerging materials for the adsorption of heavy metals and dyes. *J. Environ. Manage.* 224, 327–339.
- Siyal, A.A., Shamsuddin, M.R., Rabat, N.E., Zulfikar, M., Man, Z., Low, A., 2019. Fly ash based geopolymer for the adsorption of anionic surfactant from aqueous solution. *J. Cleaner Prod.* 229, 232–243.
- Vassilev, Stanislav V., 2013. An overview of the composition and application of biomass ash. Part I. Phase-mineral and chemical composition and classification. *Fuel* 105, 40–76.
- Tan, T.H., Mo, K.H., Ling, T.-C., Lai, S.H., 2020. Current development of geopolymer as alternative adsorbent for heavy metal removal. *Environ. Technol. Innovation* 18.
- Tang, N., Yang, K.-K., Alrefaei, Y., Dai, J.-G., Wu, L.-M., Wang, Q., 2020. Reduce VOCs and PM emissions of warm-mix asphalt using geopolymer additives. *Constr. Build. Mater.* 244.
- Tian, Q., Guo, B., Sasaki, K., 2020. Immobilization mechanism of Se oxyanions in geopolymer: Effects of alkaline activators and calcined hydrotalcite additive. *J. Hazard. Mater.* 387, 121994.
- Tian, Q., Nakama, S., Sasaki, K., 2019. Immobilization of cesium in fly ash-silica fume based geopolymers with different Si/Al molar ratios. *Sci. Total Environ.* 687, 1127–1137.
- Wang, S., Terdkiatburana, T., Tadé, M.O., 2008. Single and co-adsorption of heavy metals and humic acid on fly ash. *Sep. Purif. Technol.* 58, 353–358.
- Wang, Y., Liu, X., Zhang, W., Li, Z., Zhang, Y., Li, Y., Ren, Y., 2020. Effects of Si/Al ratio on the efflorescence and properties of fly ash based geopolymer. *J. Cleaner Prod.* 244.
- Wieszczycka, K., Filipowiak, K., Wojciechowska, I., Aksamitowski, P., 2020. Novel ionic liquid-modified polymers for highly effective adsorption of heavy metals ions. *Sep. Purification Technol.* 236.
- Xu, C., Shi, S., Wang, X., Zhou, H., Wang, L., Zhu, L., Zhang, G., Xu, D., 2020. Electrospun SiO<sub>2</sub>-MgO hybrid fibers for heavy metal removal: Characterization and adsorption study of Pb(II) and Cu (II). *J. Hazard. Mater.* 381, 120974.
- Xu, D., 2008. Adsorption of Pb(II) from aqueous solution to MX-80 bentonite: Effect of pH, ionic strength, foreign ions and temperature. *Appl. Clay Sci.* 41, 37–46.
- Yan, C., Guo, L., Ren, D., Duan, P., 2019. Novel composites based on geopolymer for removal of Pb(II). *Mater. Lett.* 239, 192–195.
- Yousef, R.I., El-Eswed, B., Alshaer, M., Khalili, F., Khoury, H., 2009. The influence of using Jordanian natural zeolite on the adsorption, physical, and mechanical properties of geopolymers products. *J. Hazard. Mater.* 165, 379–387.
- Zhu, M., Zhu, L., Wang, J., Yue, T., Li, R., Li, Z., 2017. Adsorption of Cd(II) and Pb(II) by in situ oxidized Fe<sub>3</sub>O<sub>4</sub> membrane grafted on 316L porous stainless steel filter tube and its potential application for drinking water treatment. *J. Environ. Manage.* 196, 127–136.